

Microstructure and Stray Electric Fields at Surface Cracks in Ferroelectrics

Lun Yang* and Kaushik Dayal[†]

Carnegie Mellon University

March 5, 2012

Abstract

Ferroelectric perovskites are widely used in transducer, memory and optical applications due to their attractive electromechanical and optical properties. In these brittle materials, reliability and failure of devices is dominated by the behavior of cracks. The electromechanical coupling causes cracks to interact strongly with both mechanical as well as electrical fields. Additionally, cracks and domain patterns interact strongly with each other. Hence, an understanding of the electromechanics of cracks requires an accounting of all these interactions. In this work, we apply a real-space phase-field method to compute the stresses, domain patterns, and stray electric fields in the vicinity of a stationary crack, defined here as a geometric feature that causes large but bounded stress. We investigate the effects of charge compensation on the crack face, crack orientation with respect to the crystal lattice, and applied far-field stress and electric fields.

Keywords: ferroelectrics; cracks; phase-field simulation; boundary element method; domain patterns;

1 Introduction

Ferroelectrics are widely used in sensors and actuators [25, 19], high-speed memory devices [15], microwave circuits [18, 4] and photonic switches [3] due to their attractive electromechanical and optical properties. The reliability of ferroelectrics under the complex electrical and mechanical fields that occur in these device settings is an important issue. Due to the brittle nature of ferroelectrics, failure is dominated by the electromechanics of cracks. Therefore, predicting failure requires an understanding of the interactions between cracks, domain patterns, and stress and electric fields.

There have been numerous efforts to understand the behavior of cracks in ferroelectrics and related materials. Many of these have focused on domain switching near uniformly growing cracks, e.g. [20, 7]. More recently, phase-field models have been applied to stationary cracks [24, 23, 11, 21] and also with sophisticated methods for growing cracks [1] that account elegantly for complex boundary conditions.

*luny@andrew.cmu.edu

[†]kaushik@cmu.edu

Related experimental efforts have provided much insight into the behavior of cracks, e.g. some of the more notable include [12, 22] and experiments on barium titanate single crystals using polarized light microscopy to observe individual domains [6, 5]. Many of these efforts have been reviewed in [13].

The key difference between this work and the theoretical/numerical efforts above is in our calculation of electric fields. In those works, simplifying assumptions on the surface charge and stray field are made, e.g. complete charge compensation at crack surface. While the problem of finding electric fields is posed on an infinite domain, the consequence of the simplifying assumptions is to reduce the problem to a finite domain corresponding to the ferroelectric specimen. In contrast, here we apply a recent boundary-element approach [27, 2] to accurately and efficiently account for the stray fields by consistently transforming the infinite domain problem to an equivalent finite domain problem. A consequence of this approach is that we are able to compute stray fields as well as test the effect of different assumptions on crack-face charge compensation. In terms of the energy balance between stress, electric field, anisotropy energy, and boundary conditions that determines microstructure, we account accurately for the stray electric field contribution to the balance. In addition, stray fields provide an important experimental diagnostic due to the difficulty of directly observing microstructure in the interior. For example, [14, 17] and others use Kelvin Probe Microscopy to measure stray fields in ferroelectrics.

We apply the method to compute domain patterns, stresses, and electric fields in stationary cracks at the surface of a ferroelectric under different conditions. In our work, we define the crack as a geometric notch-shaped feature that leads to large but bounded stresses (Figs. 1, 2). In particular, we investigate the role of charge compensation on the crack face, crack orientation with respect to the crystal lattice, and applied far-field stress and electric fields.

The paper is organized as follows. The model formulation and the computational method are described in Section 2. The effect of varying charge compensation is described in Section 3. The effect of applied stress and electric field is described in Section 4. The effect of different lattice orientations is described in Section 5. We conclude in Section 6.

2 Phase-Field Model and Solution Method

The potential energy E of a ferroelectric Ω with strain field ϵ and polarization field \mathbf{p} is written, following [16]:

$$E[\epsilon, \mathbf{p}] = \int_{\Omega} [U(\nabla \mathbf{p}) + W(\epsilon, \mathbf{p})] d\Omega + \frac{\epsilon_0}{2} \int_{\mathbb{R}^3} |\nabla \phi|^2 dV \quad (2.1)$$

with additional terms from loads if present. Here, U penalizes gradients in \mathbf{p} and models the energy contributions from domain walls, and the stored (Devonshire/anisotropy) energy density W penalizes \mathbf{p} and ϵ deviating from the spontaneous polarization and strain. The last term is the energy contained in the electric field $\mathbf{E} = -\nabla \phi$, where ϕ is the electric potential obtained from Maxwell's equation:

$$\nabla \cdot (\mathbf{p} - \epsilon_0 \nabla \phi) = 0 \quad \text{over } \mathbb{R}^3, \quad \text{with appropriate boundary conditions.} \quad (2.2)$$

The first two terms in E from (2.1) are local to the body being considered, while the electrostatic contribution is over all space.

Domain patterns are obtained as local minimizers of E . These minimizers are numerically calculated by starting with assumed fields ϵ, \mathbf{p} and evolving towards a minimum using a gradient flow. Unlike most

previous works in phase-field modeling, e.g. [29, 28, 26, 9, 10], we do not use the standard gradient flow based on the L_2 norm, but instead use the H_1 norm. The gradient flow of E is then:

$$\begin{aligned} \mu_1 \frac{dp_i}{dt} - \mu_2 \frac{d(p_{i,j})_{,j}}{dt} &= \left(\frac{\partial U}{\partial p_{i,j}} \right)_{,j} - \frac{\partial W}{\partial p_i} - \phi_{,i} \quad \text{over } \Omega \\ \left(\frac{\partial W}{\partial \varepsilon_{ij}} \right)_{,j} &= 0 \quad \text{over } \Omega \\ p_{i,i} - \epsilon_0 \phi_{,ii} &= 0 \quad \text{over } \mathbb{R}^3 \end{aligned} \quad (2.3)$$

with μ_1, μ_2 both non-negative. The boundary conditions for the polarization evolution (2.3)₁ are $\nabla \mathbf{p} \cdot \mathbf{n} = 0$, where \mathbf{n} is the outward normal to the boundary. The boundary conditions for mechanical equilibrium (2.3)₂ are traction-free on the bottom and top faces of the domain, specified normal tractions on the sides of the domain, and traction-free on the crack faces (Fig 2).

The boundary conditions for electrostatics (2.3)₃ are more varied. We recall that the bound surface due to polarization is $\sigma_b = \mathbf{p} \cdot \mathbf{n}$. Additionally, we can have free surface charge σ_f due to compensation from free charges in the ambient environment. The total charge on the boundary $\sigma_f + \sigma_b$. On the faces of the domain except along the crack, we assume complete compensation: $\sigma_f + \sigma_b = 0 \Leftrightarrow \sigma_f = -\mathbf{p} \cdot \mathbf{n}$. Along the crack faces, we use three models to examine the effect of charge compensation: first, we use $\sigma_f = -0.9\mathbf{p} \cdot \mathbf{n}$ that we term *complete charge compensation*; second, we use $\sigma_f = -0.5\mathbf{p} \cdot \mathbf{n}$ that we term *partial compensation*; and third, we use $\sigma_f = 0$ that we term *uncompensated*. In addition, we require that $\nabla \phi \rightarrow 0$ in the far-field and this automatically imposed by the Greens' functions of the numerical method [27].

We start with an initial polarization field that we use to obtain the strain and electric potential from (2.3)₂₃. We then update the polarization using (2.3)₁. This process is repeated until convergence.

We use tetragonal barium titanate in two-dimensions as our model material, and use the energies given in [29]:

$$\begin{aligned} U(\nabla \mathbf{p}) &= \frac{a_0}{2} (p_{1,1}^2 + p_{1,2}^2 + p_{2,1}^2 + p_{2,2}^2) \\ W(\boldsymbol{\epsilon}, \mathbf{p}) &= \frac{a_1}{2} (p_1^2 + p_2^2) + \frac{a_2}{4} (p_1^4 + p_2^4) + \frac{a_3}{2} p_1^2 p_2^2 + \frac{a_4}{6} (p_1^6 + p_2^6) + \frac{a_5}{4} p_1^4 p_2^4 \\ &\quad + \frac{1}{2} (\boldsymbol{\epsilon} - \boldsymbol{\epsilon}_T(\mathbf{p})) \cdot \mathbb{C} \cdot (\boldsymbol{\epsilon} - \boldsymbol{\epsilon}_T(\mathbf{p})) \end{aligned} \quad (2.4)$$

The polynomial in the components of \mathbf{p} in W provides a multi-well energy structure with energy wells that correspond the symmetry-related spontaneous polarizations, in this case aligned either along $(\pm 1, 0)$ or $(0, \pm 1)$. The stress-free strain $\boldsymbol{\epsilon}_T(\mathbf{p})$ is a function of polarization and represents the spontaneous strain associated with each value of polarization. Heuristically, the polynomial in W drives \mathbf{p} to preferred spontaneous variants, and the stress-free strain then prefers the strain associated to that variant. The expression for $\boldsymbol{\epsilon}_T(\mathbf{p})$ is

$$\boldsymbol{\epsilon}_T = \begin{bmatrix} \frac{(c_1 b_1 - c_2 b_2)p_1^2 + (c_1 b_2 - c_2 b_1)p_2^2}{2(c_1^2 - c_2^2)} & \frac{b_3 p_1 p_2}{c_3} \\ \frac{b_3 p_1 p_2}{c_3} & \frac{(c_1 b_2 - c_2 b_1)p_1^2 + (c_1 b_1 - c_2 b_2)p_2^2}{2(c_1^2 - c_2^2)} \end{bmatrix} \quad (2.5)$$

The reason for the H_1 -based gradient flow is that the standard L_2 gradient flow with explicit “time”-stepping requires small step size for CFL stability as a consequence of the linear diffusion-like term

from $\left(\frac{\partial U}{\partial p_{i,j}}\right)_{,j}$. With the H_1 norm, we have a second derivative on the left side that “cancels out” (in terms of CFL) the second derivative on the right in $(2.3)_1$. On taking the weak form and substituting the standard FEM ansatz in terms of shape functions, this new norm leads to a preconditioner that takes some account of the mesh. Ideally, we would set $\mu_1 = 0$ to maximize this cancellation, but this would lead to a seminorm with the boundary conditions $\nabla \mathbf{p} \cdot \hat{\mathbf{n}} = 0$, and the preconditioner would hence be singular. Hence, we use μ_1 as small as possible while retaining numerical stability of the preconditioner. The H_1 gradient flow leads to a wallclock time reduction of a factor of about 20.

The polarization update $(2.3)_1$ and mechanical equilibrium $(2.3)_2$ both use standard FEM with triangle elements and linear shape functions, and polarization and displacement are the primary variables respectively. The electrostatic equation $(2.3)_3$ needs attention as the electric fields are not confined to the ferroelectric but extend over all space. We use the boundary element approach to solve the infinite domain problem efficiently and accurately, as described in [2, 27]. In particular, [27] describes a new iterative formulation that is particularly suited for nonlinear coupled problems such as arise here.

The generic geometry that we will consider in this paper is shown in Fig. 1 together with discretization, boundary conditions and initial polarization. The mesh is refined near the crack tip. We note that the crack geometry is set up so that while there are large stresses, these are bounded and do not require special treatment.

3 Effect of Charge Compensation on the Crack Surface

The domain patterns near the crack tip involve a balance between elastic energy, the electrostatic energy, gradient energy, and the energy due to the polarization deviating from the preferred states. In a generic complex geometry, it is not possible to minimize each individually; for example, minimizing the electrostatic energy requires \mathbf{p} to be tangential to the boundary everywhere to avoid bound surface charges, but this will obviously force the polarization to deviate from the preferred state. It is this particular aspect that we study in this section by varying the charge compensation on the crack face. This forces a competition between anisotropy energy, minimizing bound charges in the interior as well as on the surface with a complex geometry, and finally the complex stress fields due to the crack.

The complex orientation of the crack surface provides domain patterns that must balance all the energetic contributions. We recall that the surface bound charge due to a terminating polarization is $\mathbf{p} \cdot \mathbf{n}$. To examine the effect of charge compensation on the crack face, we use three models: complete charge compensation, partial compensation, uncompensated. And the top free surface excluding the crack, we assume the surface charge is completely compensated. In this section, we assume there is no applied far-field stress or electric field, that is $\sigma_0 = 0$ and $E_0 = 0$ in Fig. 1. We assume traction-free mechanical boundary conditions both at the top free surface and over the crack surface. In all cases, we use \mathbf{p} aligned along the horizontal direction as initial condition.

Crack face electrical boundary conditions are usually assumed to be impermeable (no electric field in the gap), permeable (the crack does not perturb the electric field and is closed), and other cases between these extremes [8]. In a sense, the notion of crack permeability is related to the best approximate crack-face boundary condition to be used when solving electrostatics only on the body rather than all space. Because our approach solves for the external fields in all space, we do not use approximate crack-face conditions and it is not possible to make a direct comparison between our surface compensation approach and the

approximate conditions. However, since we neither make the assumption that fields in the crack are zero, nor do we assume that the field is unperturbed by the crack, the closest case to our setting appears to be semipermeable. A related issue is the fact that uncompensated charges on opposite crack faces cause mechanical tractions. The energy expression includes energetic contributions due to charge distribution. In the finite deformation context, this traction would appear simply by minimizing the energy with respect to displacement and polarization, as the minimization would include the energetic effect of moving the charges on the opposite sides of the crack face with respect to each other. In the small deformation approximation that we are using, this traction is not present and we have not added it separately.

In the completely compensated case, the domain pattern is fairly simple, Fig. 2. The initial condition is fairly low energy and there are only small energetic contributions both from the interior and the crack surface. Hence, the equilibrium state is quite close to starting guess.

We then examine the domain patterns with uncompensated charges. In this setting, the initial guess has small energetic contributions from the interior, but has large uncompensated bound charges on the crack surface due to normal termination of \mathbf{p} . Fig. 3(a) shows the equilibrium domain pattern near the crack tip. The electrostatic energy dominates in this setting. As can be seen from Fig. 3(a), \mathbf{p} aligns tangential to the crack surface, and two 90° domain walls form on both sides of the crack. Also, the magnitude of \mathbf{p} increases in the region directly below the crack due to the large electric fields and stresses, Figs. 4(c) and 4(a) respectively. As these latter figures show, the largest Von Mises stress and electric field are observed near the crack tip; besides these, relatively large stresses are observed in the region between the 90° walls, while large electric fields occur outside the material in the crack gap.

Finally, we examine the domain patterns with partial compensation. Polarization at the crack surface becomes partially tangential to balance the electrostatic energy with the anisotropy energy, Fig. 3(b). Similar to the completely uncompensated case, the magnitude of \mathbf{p} increases in the region directly below the crack tip. However, 90° domain walls are not observed. While the largest Von Mises stress and electric fields are observed near the crack tip, Figs. 4(d) and 4(b) respectively, the magnitudes of both quantities are much smaller than observed in the completely uncompensated setting.

4 Effect of Far-field Applied Stress and Electric Field

In this section, we describe the effect of far-field applied normal stress and electric field, oriented as shown in Fig. 1.

First, we apply different values of far-field tensile stress σ_0 and focus on the consequent change in the maximum Von Mises stress in the ferroelectric and maximum electric field both inside and outside the ferroelectric. We do this with the three different charge compensations described in Section 3. Figs. 5(a) and 5(b) show the normalized maximum Von Mises stress and the maximum electric field respectively for different values of σ_0 . The normalization is with respect to the maximum Von Mises stress and electric field without applying any stress or electric field.

As expected, the maximum Von Mises stress increases with σ_0 . The influence of different levels of charge compensation is also clearly felt as the increase is much larger when the charge is completely compensated, Fig. 5(a). Similarly, the increase in the maximum electric field is also larger when the charge is completely compensated, Fig. 5(b). The heuristic reason for this observation is that when the surface charge is not compensated, the formation of 90° domain walls and polarization switching provide

a means for the specimen to accommodate the applied loads. Fig. 6 shows the domain pattern, the Von Mises stress and the electric potential with no charge compensation when $\sigma_0 = 0.2$ (normalized). Both \mathbf{p} and ϕ are comparable to Figs. 3(a) and 4(c) with no applied stress. However, the Von Mises stress in Fig. 6(b) is significantly higher than in Fig. 4(a). We also notice that the maximum electric field decreases slightly as σ_0 increases for $\sigma_0 \lesssim 0.2$ for both partially compensation and uncompensated, Fig. 5(b). However, as σ_0 increases beyond 0.2, the electric field increases for partial compensation, while it continues to decrease if uncompensated.

Second, we apply a far-field electric field E_0 and study the effect on the maximum stress and electric field. Again, we compare the role of the three different levels of charge compensation. In general, E_0 induces only small changes in both the stress and electric field, Fig. 7(a) and 7(b). This is consistent with the experimental observations of [17] on a configuration that is very similar to our calculation. In particular, they too find that applied in-plane electric fields have little effect on the key features of the stray field. We also compare the polarization, stress and potential field with applied field, Fig. 8, with Figs. 3(a), 4(a) and 4(c) that are computed in the absence of applied field and note that the changes are minor. However, different levels of charge compensation result in significantly different response of the stress and electric field when E_0 increases. Both the stress and electric field increase with increasing E_0 when the charge is completely or partially compensated, Figs. 7(a) and 7(b). When uncompensated, both the stress and electric field initially slightly decrease and then slightly increase as E_0 increases; however, all these changes are small in comparison to the completely and partially compensated cases. Qualitatively, as with mechanical loading, the ferroelectric is able to accommodate applied electrical loading better when the electrostatic boundary conditions are less constraining as in the case of complete compensation.

5 Effect of Crack Orientation with Respect to Crystal Lattice

In this section, we study the effect of the crack orientation with respect to the crystal lattice, by varying the orientation of the computational domain as in Fig. 9. In addition to the case of the crystal lattice oriented along the free surface ($\theta = 0^\circ$) in previous sections, here we examine relative orientations of $\theta = 15^\circ$ and $\theta = 30^\circ$.

Figs. 10(a) and 10(b) show the domain patterns for $\theta = 15^\circ$ and $\theta = 30^\circ$ respectively with no charge compensation. For $\theta = 15^\circ$, we see two distinct 90° domain walls on the left side of the crack. In addition, the magnitude of \mathbf{p} increases in the region beneath the crack. When $\theta = 30^\circ$, the domain structure on the right side of the crack is indistinct, whereas prominent 90° domain walls form on the left side. Fig. 11(a), for $\theta = 15^\circ$, and Fig. 4(a), for $\theta = 0^\circ$, show that the stress fields in these cases are similar. On increasing θ to 30° , Fig. 11(b), we find a significant region of high stress developing on the left side of the crack. Figs. 11(c) and 11(d) show the electric potential field for these cases.

Figs. 12(a) and 12(b) show the domain patterns for $\theta = 15^\circ$ and $\theta = 30^\circ$ respectively with partial compensation. The polarization field adjusts slightly to the presence of the crack but does not form any distinct 90° domain walls in either case. Fig. 13 shows that both stress and electric potential are much smaller compared to the case with no charge compensation, Fig. 11.

6 Conclusion

We have applied a real-space phase field method that can handle the stray electric fields to compute the microstructure in ferroelectrics with a crack with different levels of surface charge compensation. We have examined the effect the applied stress, electric field as well as crack orientation relative to crystal lattice on the domain patterns, stress fields, and stray electric fields in the crack vicinity. We find that the electrostatic energy dominates the energy balance if the surface charge on the crack face is not compensated. We find the formation of 90° domain walls on both sides of the crack in this situation. When far-field stress or electric field is applied, the microstructure is less sensitive to the applied field when the charge is completely compensated and hence the material has a larger response to applied field. In the same setting with no charge compensation, the boundary conditions allow some accommodation of the applied loads and hence the material response is smaller. In the case of different crack/lattice orientations, we find again that charge compensation plays a qualitatively similar role.

Acknowledgment

This research was supported in part by the National Science Foundation through TeraGrid resources provided by the Pittsburgh Supercomputing Center. The real-space phase-field program described above is available at www.matforge.org. We thank Christoph Ortner for suggesting the H_1 -based gradient flow.

References

- [1] Amir Abdollahi and Irene Arias. Phase-field modeling of the coupled microstructure and fracture evolution in ferroelectric single crystals. *Acta Materialia*, 59(12):4733 – 4746, 2011.
- [2] K. Dayal and K. Bhattacharya. A real-space non-local phase-field model of ferroelectric domain patterns in complex geometries. *Acta Materialia*, 55(6):1907–1917, 2007.
- [3] K. Dayal and K. Bhattacharya. Active tuning of photonic device characteristics during operation by ferroelectric domain switching. *J. Appl. Phys.*, 102:064102, 2007.
- [4] M. Y. El-Naggar, K. Dayal, D. G. Goodwin, and K. Bhattacharya. Graded ferroelectric capacitors with robust temperature characteristics. *J. Appl. Phys.*, 100:114115, 2006.
- [5] D. Fang, Y. Jiang, S. Li, and CT Sun. Interactions between domain switching and crack propagation in poled batio3 single crystal under mechanical loading. *Acta Materialia*, 55(17):5758–5767, 2007.
- [6] Y. Jiang, Y. Zhang, B. Liu, and D. Fang. Study on crack propagation in ferroelectric single crystal under electric loading. *Acta Materialia*, 57(5):1630–1638, 2009.
- [7] C.M. Landis. On the fracture toughness of ferroelastic materials. *Journal of the Mechanics and Physics of Solids*, 51(8):1347–1369, 2003.
- [8] C.M. Landis. Energetically consistent boundary conditions for electromechanical fracture. *International journal of solids and structures*, 41:6291-6315, 2004.

- [9] LJ Li, CH Lei, YC Shu, and JY Li. Phase-field simulation of magnetoelastic couplings in ferromagnetic shape memory alloys. *Acta Materialia*, 2011.
- [10] LJ Li, Y. Yang, YC Shu, and JY Li. Continuum theory and phase-field simulation of magnetoelectric effects in multiferroic bismuth ferrite. *Journal of the Mechanics and Physics of Solids*, 58(10):1613–1627, 2010.
- [11] W. Li and C.M. Landis. Nucleation and growth of domains near crack tips in single crystal ferroelectrics. *Engineering Fracture Mechanics*, 2011.
- [12] C.S. Lynch. Fracture of ferroelectric and relaxor electro-ceramics: influence of electric field1. *Acta materialia*, 46(2):599–608, 1998.
- [13] G.A. Schneider. Influence of electric field and mechanical stresses on the fracture of ferroelectrics. *Annual Review of Materials Research*, 37(1):491, 2007.
- [14] GA Schneider, F. Felten, and RM McMeeking. The electrical potential difference across cracks in pzt measured by kelvin probe microscopy and the implications for fracture. *Acta materialia*, 51(8):2235–2241, 2003.
- [15] J.F. Scott. *Ferroelectric memories*. Springer Verlag, 2000.
- [16] YC Shu and K. Bhattacharya. Domain patterns and macroscopic behaviour of ferroelectric materials. *Philosophical Magazine Part B*, 81(12):2021–2054, 2001.
- [17] X. Sun, YJ Su, KW Gao, LQ Guo, LJ Qiao, WY Chu, and T.Y. Zhang. Surface potential distribution in an indentation-pre-cracked batio3 single crystal. *Journal of the American Ceramic Society*.
- [18] A. K. Tagantsev, V. O. Sherman, K. F. Astafiev, J. Venkatesh, and N. Setter. Ferroelectric materials for microwave tunable applications. *J. Electroceram.*, 11:5–66, 2003.
- [19] K. Uchino. *Piezoelectric Actuators and Ultrasonic Motors*. Kluwer, 1996.
- [20] J. Wang and C.M. Landis. On the fracture toughness of ferroelectric ceramics with electric field applied parallel to the crack front. *Acta materialia*, 52(12):3435–3446, 2004.
- [21] J. Wang and T.Y. Zhang. Phase field simulations of polarization switching-induced toughening in ferroelectric ceramics. *Acta materialia*, 55(7):2465–2477, 2007.
- [22] I. Westram, W.S. Oates, D.C. Lupascu, J. Rodel, and C.S. Lynch. Mechanism of electric fatigue crack growth in lead zirconate titanate. *Acta materialia*, 55(1):301–312, 2007.
- [23] B.X. Xu, D. Schrade, D. Gross, and R. Mueller. Fracture simulation of ferroelectrics based on the phase field continuum and a damage variable. *International journal of fracture*, pages 1–10, 2010.
- [24] B.X. Xu, D. Schrade, D. Gross, and R. Mueller. Phase field simulation of domain structures in cracked ferroelectrics. *International journal of fracture*, 165(2):163–173, 2010.
- [25] Y. Xu. *Ferroelectric materials and their applications*. North-Holland, 1991.
- [26] L. Yang and K. Dayal. Formulation of phase-field energies for microstructure in complex crystal structures. *Applied Physics Letters*, 96:081916, 2010.

- [27] Lun Yang and Kaushik Dayal. A completely iterative method for the infinite domain electrostatic problem with nonlinear dielectric media. *Journal of Computational Physics*, 230(21):7821 – 7829, 2011.
- [28] Lun Yang and Kaushik Dayal. Effect of lattice orientation, surface modulation, and applied fields on free-surface domain microstructure in ferroelectrics. *Acta Materialia*, 59(17):6594 – 6603, 2011.
- [29] W. Zhang and K. Bhattacharya. A computational model of ferroelectric domains. part i: model formulation and domain switching. *Acta materialia*, 53(1):185–198, 2005.

Figures

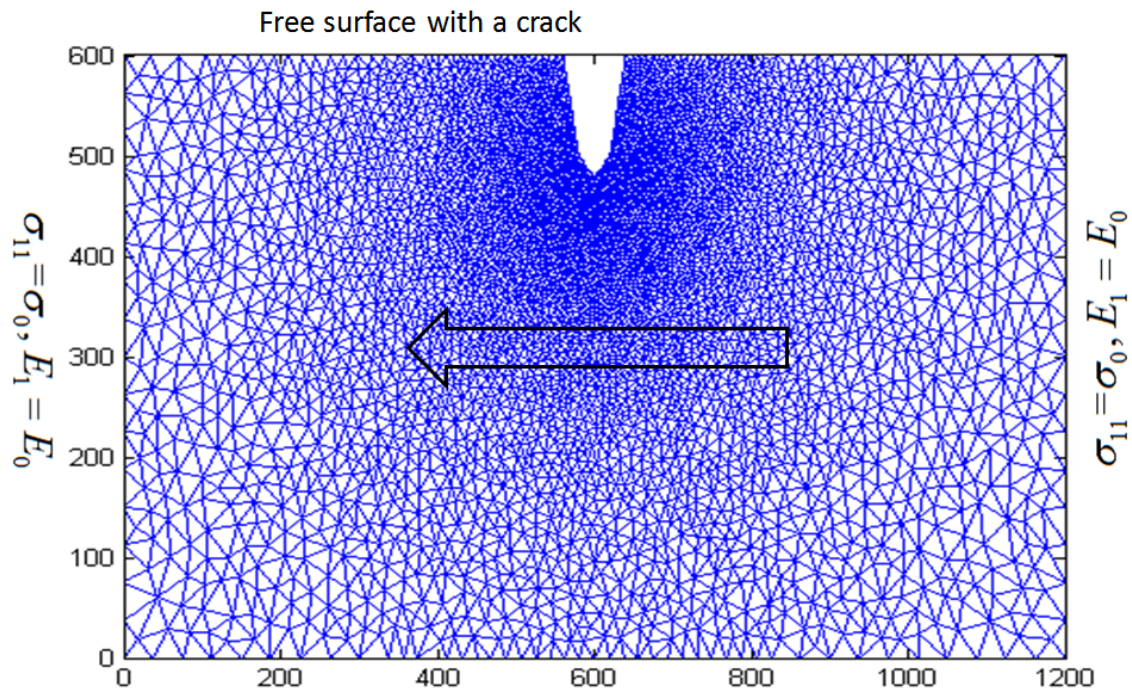


Figure 1: Computational domain geometry, discretization and boundary conditions. Note that the crack shape in this figure is accurate, whereas the jagged shapes in subsequent figures are an artifact of the visualization software.

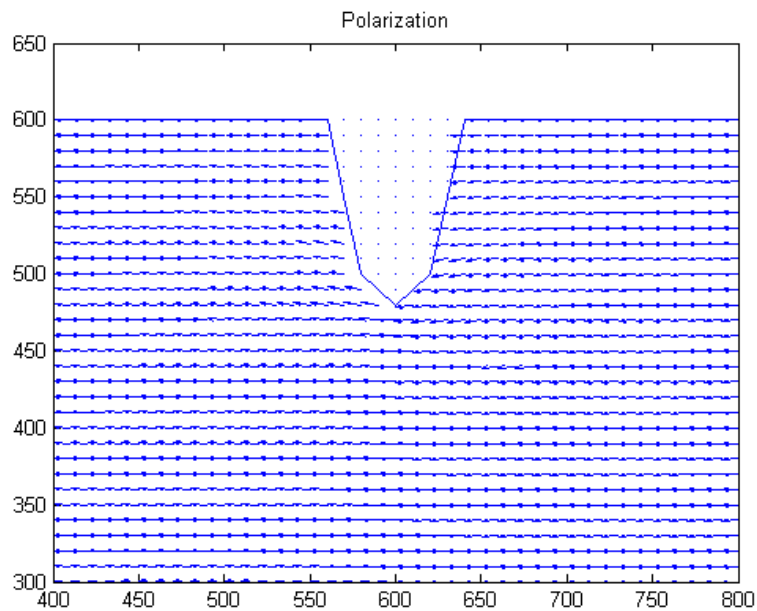


Figure 2: Domain pattern with complete charge compensation on the crack surface.

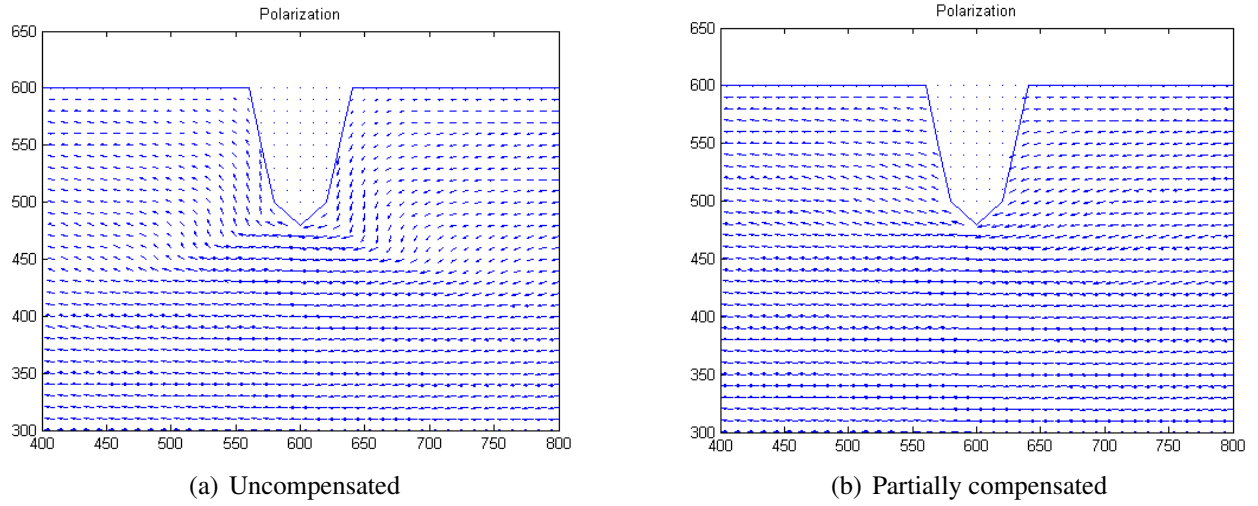


Figure 3: Domain pattern with different charge compensation on the crack surface.

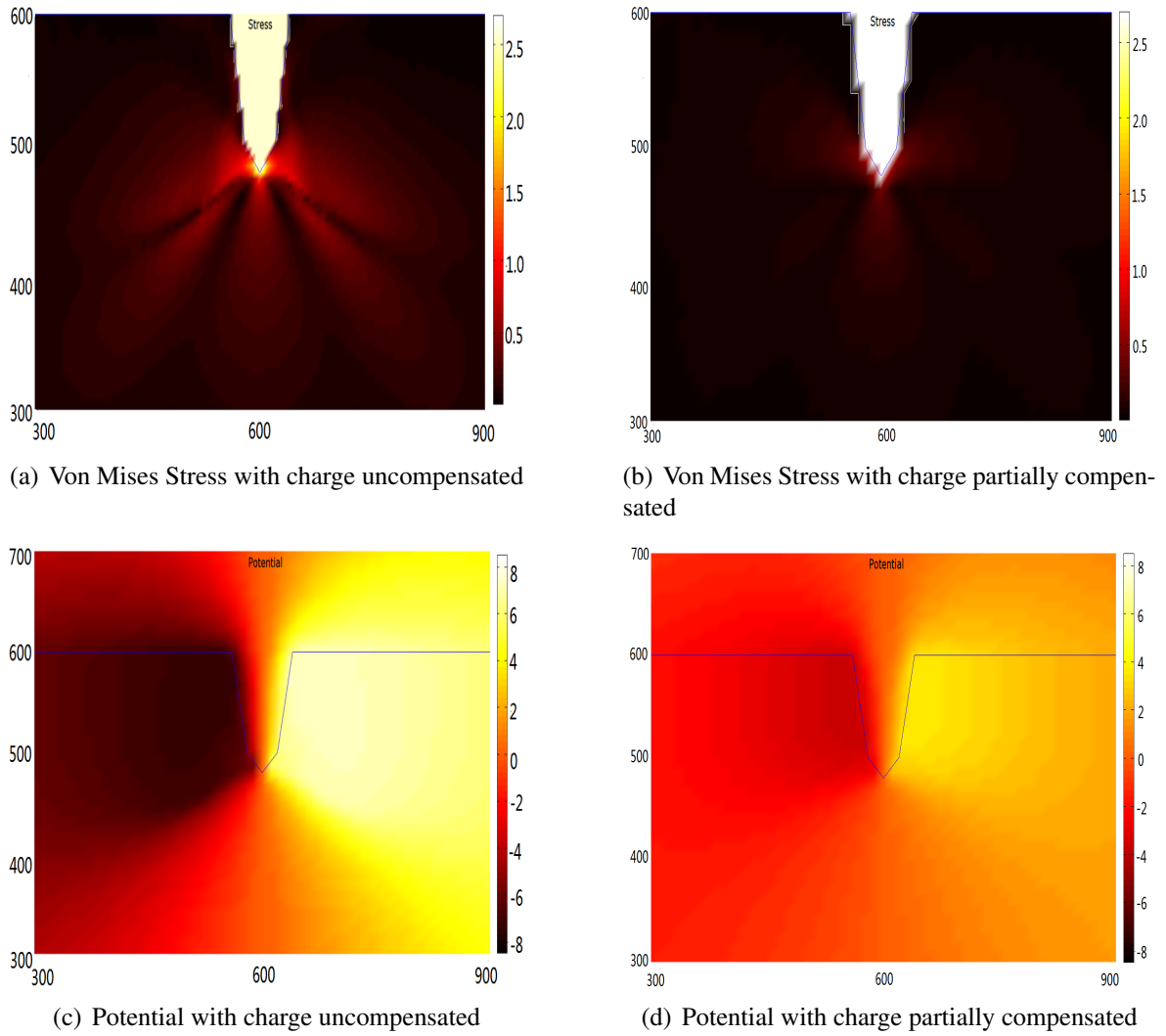
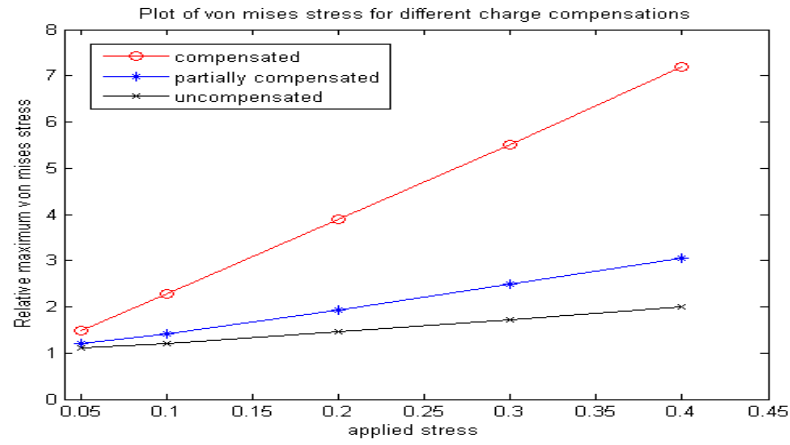
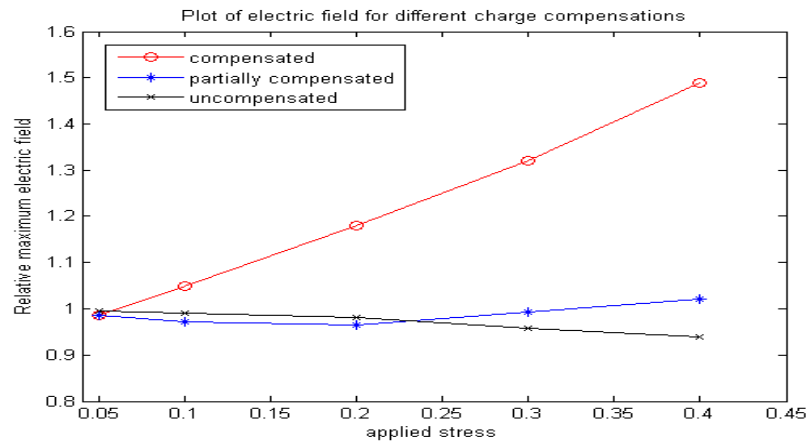


Figure 4: Stress and potential fields with different charge compensation on the crack surface.

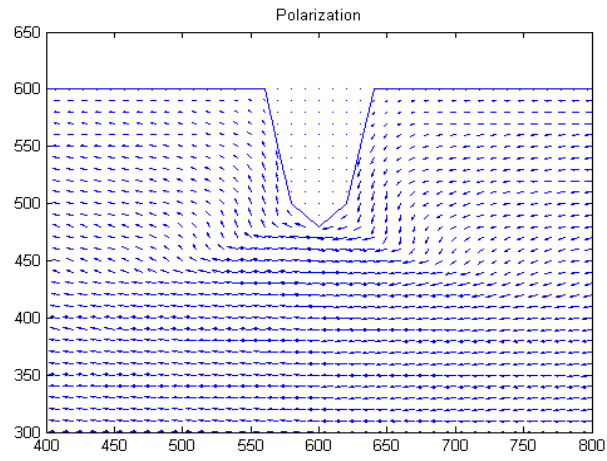


(a) Maximum Von Mises Stress

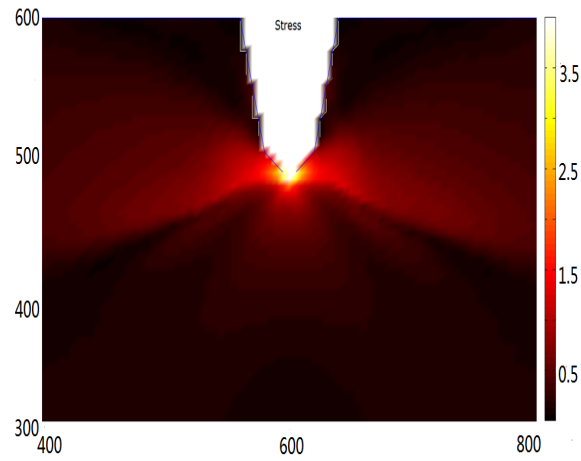


(b) Maximum Electric Field

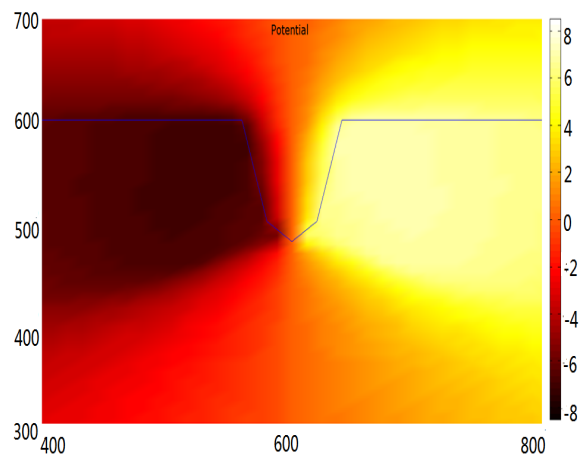
Figure 5: Maximum stress and electric field with applied tensile stress σ_0 .



(a) Polarization

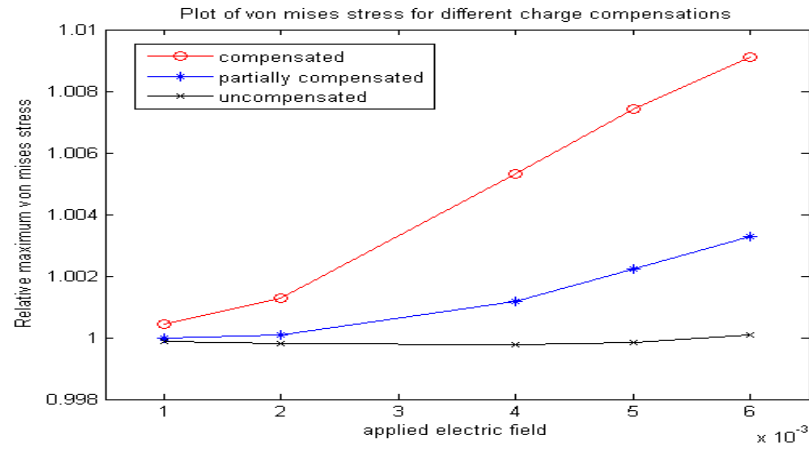


(b) Stress

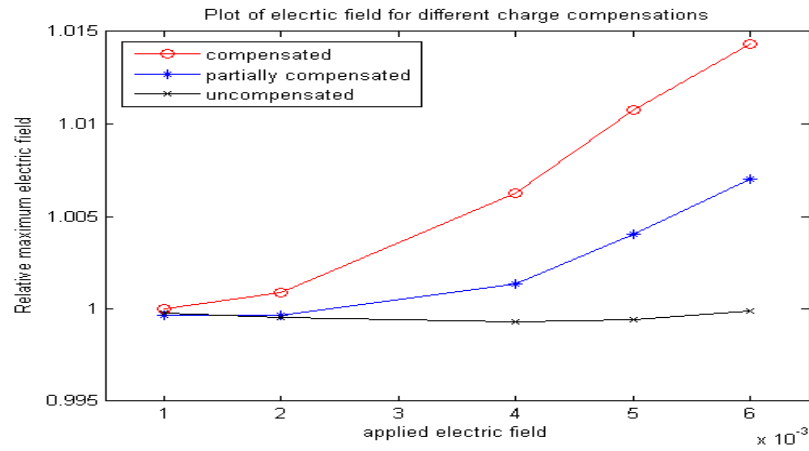


(c) Potential

Figure 6: Polarization, stress and potential without charge compensation on the crack surface when $\sigma_0 = +0.2$.

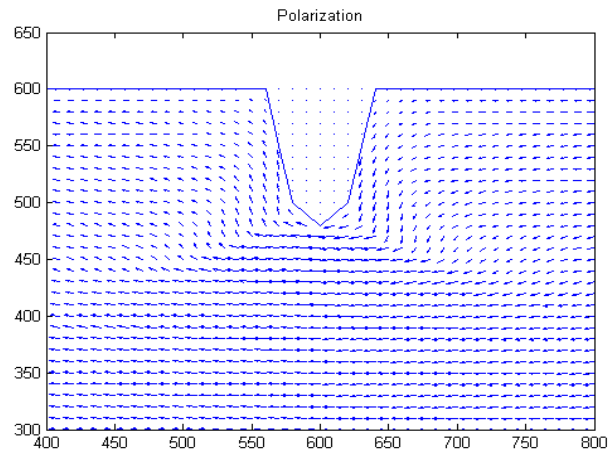


(a) Maximum Von Mises Stress

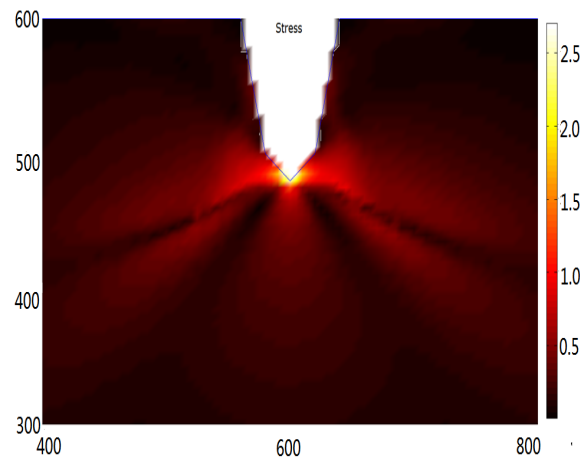


(b) Maximum Electric Field

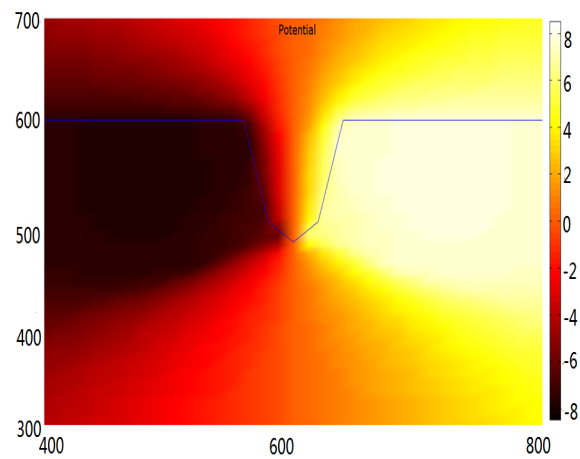
Figure 7: Maximum stress and electric field with applied far-field electric field E_0 .



(a) Polarization



(b) Stress



(c) Potential

Figure 8: Polarization, stress and potential without charge compensation on the crack surface when $E = 0.004$.

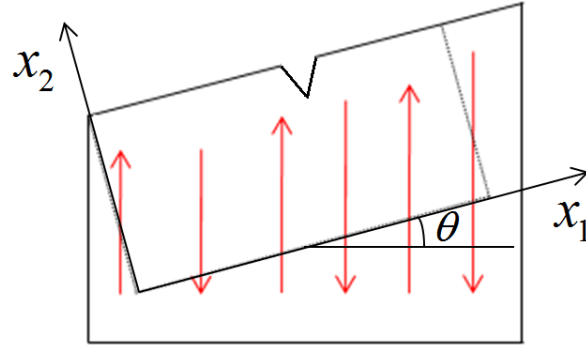


Figure 9: Crack orientation relative to crystal lattice and computational domain.

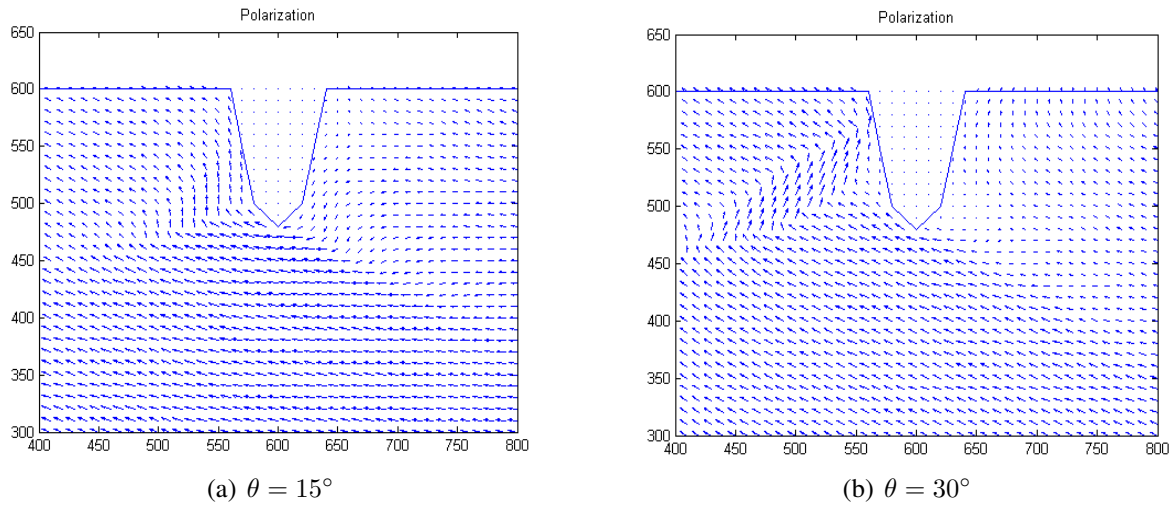


Figure 10: Domain patterns without charge compensation on the crack surface with different lattice orientations.

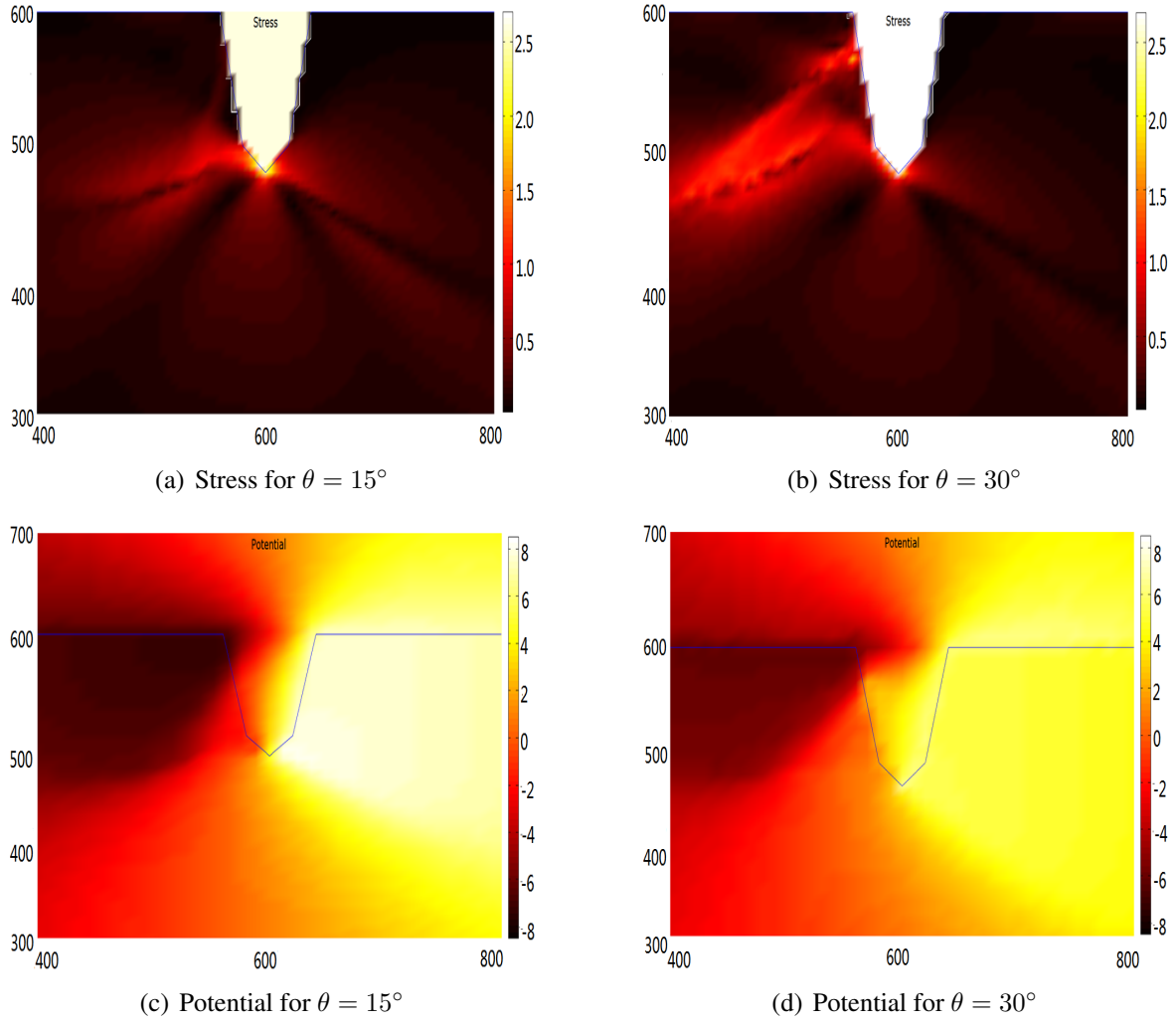


Figure 11: Stress and electric potential fields without charge compensation on the crack surface with different lattice orientations.

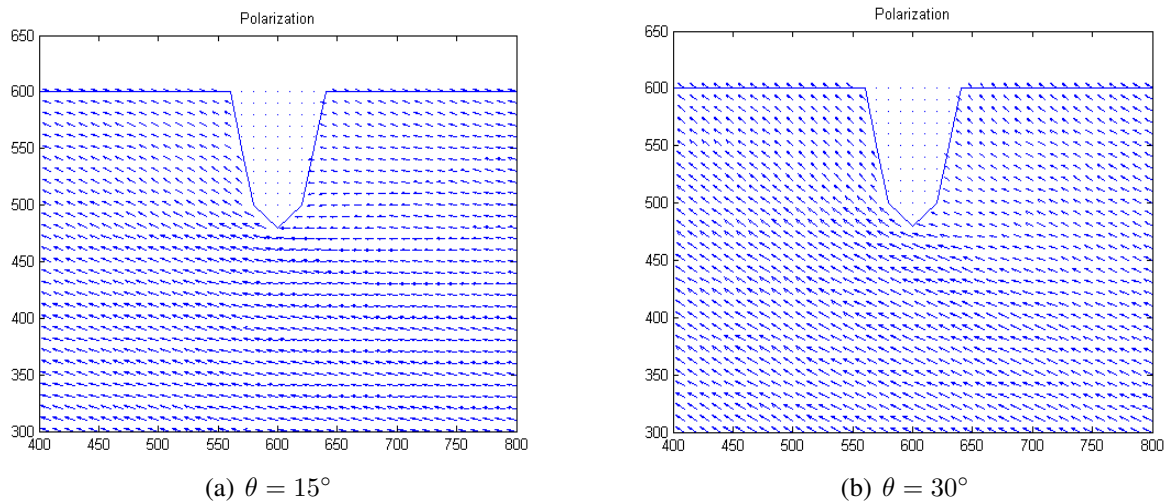


Figure 12: Domain patterns with partial charge compensation on the crack surface with different lattice orientations.

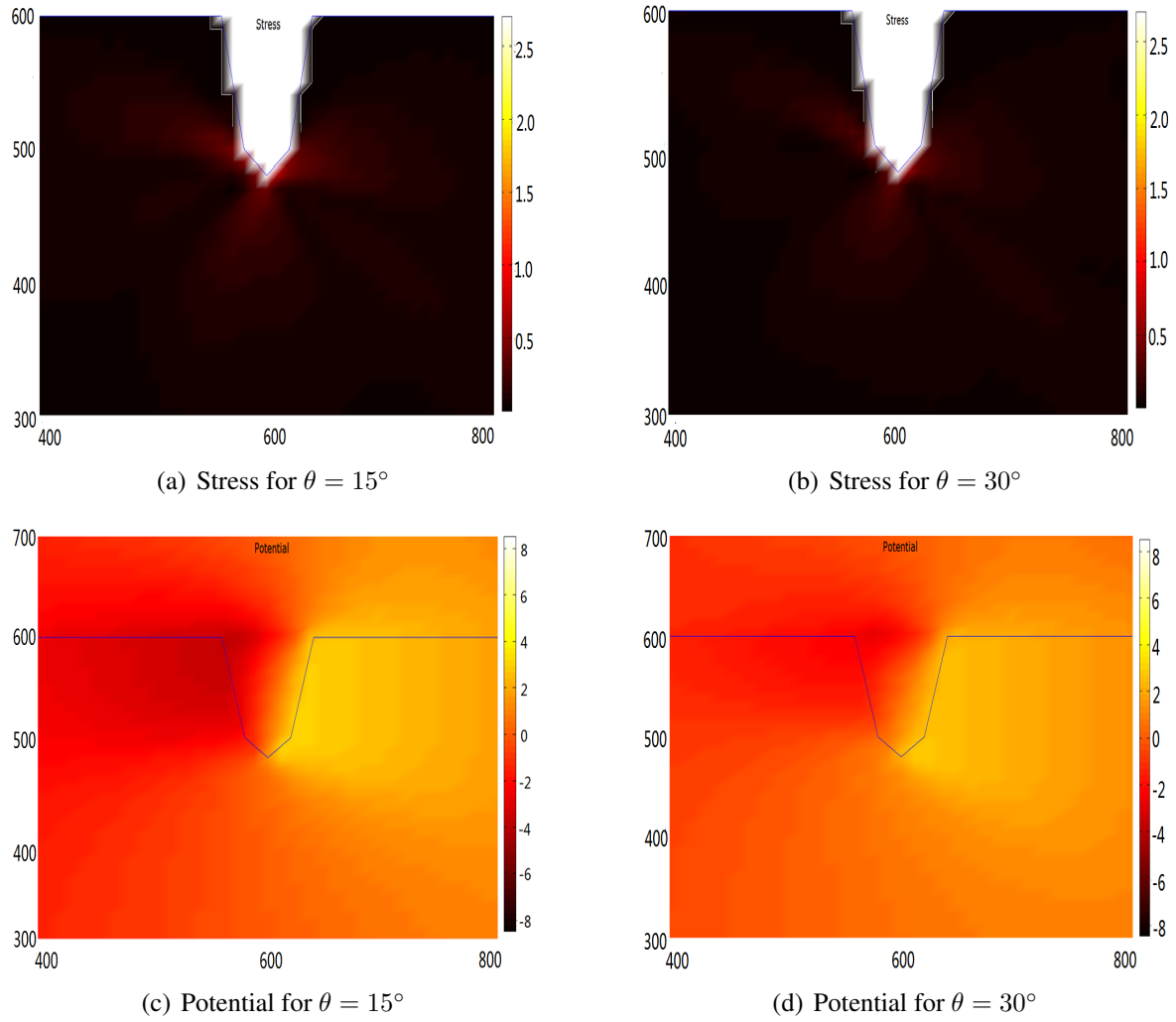


Figure 13: Stress and electric potential fields with partial charge compensation on the crack surface with different lattice orientations.